Macromolecular Research
https://doi.org/10.1007/s13233-025-00488-2

ARTICLE

Solvent-driven self-assembly of amphiphilic block copolymers in emulsions for hierarchical particle design

Juyoung Lee[1] · Hayoung Kim[1] · Hyeong Seok Oh[1] · Kang Hee Ku[1]

Received: 12 November 2025 / Revised: 12 December 2025 / Accepted: 27 December 2025

Abstract

The spatial organization of amphiphiles within emulsions offers a versatile route to constructing complex soft-matter architectures. Here, we present the solvent-dependent interfacial behavior of polystyrene-*block*-poly(4-vinylpyridine) (PS-*b*-P4VP) copolymers in evaporative emulsions and its decisive role in dictating particle morphology. By systematically varying the solvent selectivity toward each block, we achieve precise control over the confined assembly of PS-*b*-P4VP, producing a continuous morphological evolution from nonporous spheres to porous particles, vesicles, and micellar structures. Enhanced affinity of solvents for the P4VP block promotes the polymer adsorption at the emulsion interface, triggering pronounced interfacial instabilities that drive hierarchical structure formation. Furthermore, variations in P4VP volume fraction and surfactant concentration modulate these interfacial dynamics, enabling a tunable library of well-defined polymer particles. This study establishes solvent selectivity as a powerful design parameter for manipulating interfacial self-assembly pathways of amphiphilic block copolymers, offering a robust and scalable strategy for engineering functional soft colloids.

Graphical abstract

Solvent selectivity directs the interfacial self-assembly of PS-*b*-P4VP within evaporative emulsions, yielding diverse morphologies from porous spheres to vesicles and micellar aggregates. Enhanced P4VP-affinity solvents promote interfacial adsorption and instability, enabling tunable hierarchical particles through controlled solvent, surfactant, and composition parameters

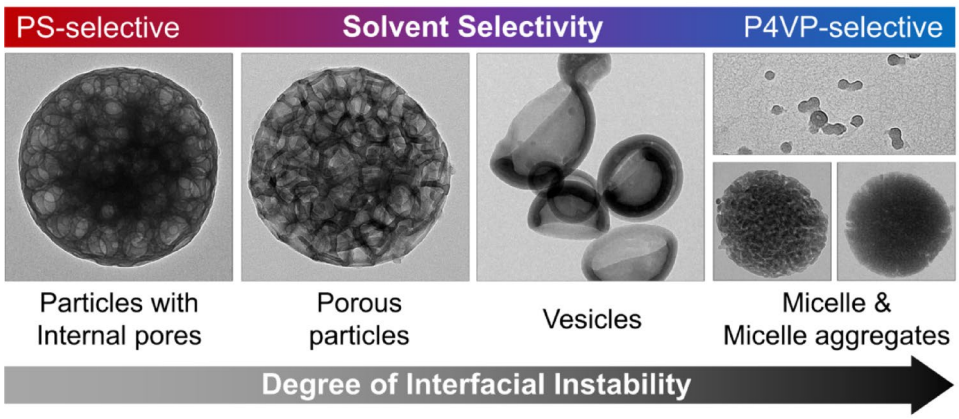

Keywords Amphiphilic block copolymers · Interfacial instability · Solvent selectivity · Porous particles · Emulsions

Juyoung Lee and Hayoung Kim have contributed equally to this work.

Extended author information available on the last page of the article

Published online: 04 February 2026

1 Introduction

Amphiphilic molecules are fundamental building blocks for constructing supramolecular architectures that underpin a wide range of applications, including biomedicine, soft sensors, nanoreactors, and separation membranes [1–5]. The ability to precisely manipulate their microphase separation enables the creation of complex and functional morphologies [6–9]. Among these systems, the solvent-mediated self-assembly of block copolymers (BCPs) confined within emulsion droplets has emerged as a particularly powerful and scalable route for fabricating polymer particles with programmable shapes, dimensions, and internal nanostructures [10–16]. The deformable nature of the emulsion interface allows dynamic restructuring during solvent evaporation, giving rise to an exceptional diversity of morphologies such as ellipsoidal, patchy, or bud-like particles [17–22].

In these emulsions, the co-adsorption of amphiphilic BCPs and surfactants at the oil/water interface significantly lowers the interfacial tension, leading to interfacial instability: a key driving force for morphological transformation [23–26]. Such interfacial phenomena have enabled the formation of hierarchically organized architectures, including vesicles [27], porous particles [28], and micellar assemblies [29], using well-defined amphiphilic systems such as polystyrene-*block*-poly(4-vinylpyridine) (PS-*b*-P4VP) and polystyrene-*block*-poly(ethylene oxide) (PS-*b*-PEO). Despite these advances, systematic understanding of how the hydrophilic-lipophilic balance of amphiphilic BCPs governs their interfacial activity and resultant structures within emulsions remains limited.

During solvent evaporation, the confined self-assembly of BCPs is strongly influenced by the diffusion kinetics and solubility gradients of the organic solvent [11]. The spatial solvent concentration profile across the droplet dictates both the orientation and packing of BCP domains at the interface, ultimately determining the particle morphology [30, 31]. For example, in toluene-based emulsions of polystyrene-*block*-polybutadiene (PS-*b*-PB), rapid solvent loss generates steep concentration gradients, driving the alignment of polymer chains perpendicular to the droplet surface and yielding non-spherical particles [32]. Moreover, the extent of BCP chain swelling and their adsorption at the oil/water boundary are highly sensitive to solvent polarity [33]. For example, hydrophobic solvents tend to stabilize micellar structures with hydrophilic cores and hydrophobic coronas [34, 35], suppressing their interfacial adsorption [36]. Yet, the interplay between solvent selectivity, interfacial instability, and BCP assembly under evaporative confinement remains poorly resolved.

Here, we elucidate the solvent-directed structural evolution of PS-*b*-P4VP particles formed via confined assembly in evaporative emulsions. A series of organic solvents with distinct affinities for each block are employed to modulate the interfacial adsorption of PS-*b*-P4VP and thereby regulate the degree of interfacial instability. Enhanced solvent selectivity toward P4VP promotes strong BCP adsorption at the droplet interface, leading to a continuous morphological transition from internally porous spheres to vesicles and micellar aggregates. Furthermore, we systematically investigate how P4VP volume fraction and surfactant concentration cooperatively influence interfacial dynamics and the resulting shape transformations. Collectively, this study reveals solvent selectivity as a powerful design parameter for programming the interfacial self-assembly pathways of amphiphilic BCPs, providing general insights for the rational design of hierarchical polymer colloids.

2 Experimental

2.1 Materials

Cyclohexane (≥99%), benzene (≥99%), toluene (≥99.5%), dichloromethane (≥99.5%), chloroform (≥99%), 1-butanol (≥99.4%), 1-pentanol (≥99%), 1-hexanol (≥99%), and sodium dodecyl sulfate (SDS, ≥99%) were purchased from Sigma-Aldrich and were used as received. The following PS-*b*-P4VP BCPs were purchased from Polymer Source Inc.: PS_{116k}-*b*-$P4VP_{4k}$ (dispersity ($Đ$) = 1.07), PS_{40k}-*b*-$P4VP_{5.6k}$ ($Đ$ = 1.1), PS_{27k}-*b*-$P4VP_{7k}$ ($Đ$ = 1.15), PS_{50k}-*b*-$P4VP_{18k}$ ($Đ$ = 1.15), PS_{15k}-*b*-$P4VP_{7k}$ ($Đ$ = 1.18), and $PS_{9.8k}$-*b*-$P4VP_{10k}$ ($Đ$ = 1.08), where the subscripts imply the number-average molecular weights of each block.

2.2 Preparation of PS-*b*-P4VP BCP particles

A homogeneous polymer solution of PS-*b*-P4VP (1 wt%) was prepared by dissolving the polymer in an appropriate organic solvent and stirring at room temperature for over 12 h. The resulting solution (0.2 mL) was emulsified with 2 mL of an aqueous SDS solution (typically 0.4 wt%) using a high-speed homogenizer operated at 20,500 rpm for 1 min. The resulting emulsions were gently stirred at ambient temperature for 48 h to allow complete solvent evaporation and particle solidification. The obtained particles were purified by repeated centrifugation (11,000 rpm, 10 min, three cycles) with deionized (DI) water to remove residual surfactants and subsequently redispersed in DI water for further characterization.

2.3 Characterization

The morphological evolution of PS-*b*-P4VP particles during solvent evaporation was monitored using optical microscopy (Ti2-U, Nikon). In particular, the time-resolved formation of vesicular structures was investigated for dichloromethane-based emulsions containing PS_{27k}-*b*-$P4VP_{7k}$. Surface and internal morphologies of the resulting particles were examined by field-emission scanning electron microscopy (FE-SEM; Hitachi SU8200) and transmission electron microscopy (TEM; FEI Tecnai G2 F20T and JEOL JEM-2100F). For SEM analysis, particle suspensions were drop-cast onto Si wafers and dried under ambient conditions. TEM samples were prepared by depositing the particle dispersion onto carbon-coated copper grids, followed by exposure to iodine vapor to selectively stain the P4VP domains. To trace the time-dependent formation of micellar aggregates in butanol-based emulsions, aliquots were withdrawn after 1, 4, 12, and 20 h of solvent evaporation and subsequently freeze-dried (− 120 °C, 5 mTorr; Ilsinbiobase FD 12008).

3 Results and discussion

A series of PS-*b*-P4VP particles were prepared through emulsification of polymer solutions (200 µL, 10 mg mL^{-1}) with an aqueous SDS solution (2 mL, 0.4 wt%) using a high-speed homogenizer operated at 20,500 rpm. The resulting emulsions were stirred gently at room temperature for 48 h to allow complete solvent evaporation, yielding solidified BCP particles (Scheme 1). The anionic surfactant SDS was selected to achieve balanced co-adsorption with the amphiphilic BCPs at the oil/water interface [26, 37], a key factor governing the extent of interfacial instability. Throughout this study, the surfactant concentration was fixed at C_{SDS}=0.4 wt%, unless otherwise noted, to ensure reproducible interfacial conditions. To systematically probe the effect of solvent quality on the confined assembly of PS-*b*-P4VP, we employed a series of organic solvents exhibiting distinct selectivities toward the individual blocks. Representative photographs of polymer solutions and emulsions, showing solvent-dependent turbidity and its evolution during solvent evaporation, are provided in the Supporting Information (Figures S1 and S2). The degree of solvent selectivity was quantitatively estimated using the polymer–solvent interaction parameter (χ), which correlates with the solubility parameters (δ) of each component according to the relation $\chi \propto (\delta_{solvent} - \delta_{block})^2$ [38]. Larger deviations in δ indicate poorer solubility and thus higher selectivity. The calculated solubility parameters (δ_t) of the solvents used in this work are summarized in Table 1, providing a quantitative basis for correlating solvent affinity with the observed interfacial behavior [39].

3.1 Effect of solvent selectivity: PS-selective solvent

Figure 1 shows the SEM and TEM images of PS_{27k}-*b*-$P4VP_{7k}$ particles assembled in emulsions containing three PS-selective organic solvents: cyclohexane, toluene, and benzene. Spherical particles formed from cyclohexane exhibit smooth surfaces and well-defined internal pores with an average diameter of 87 ± 11 nm (Fig. 1a, b). These structures consist of a PS-rich interior framework encapsulated by a thin P4VP layer on both the outer surface and pore walls. Given that the δ values of PS and P4VP

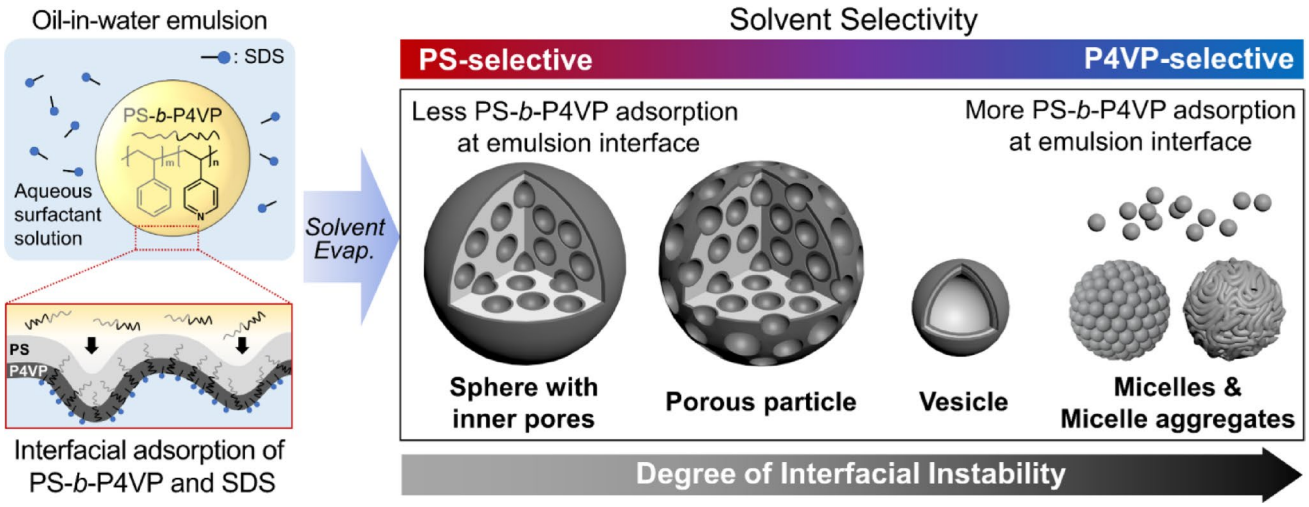

Scheme 1 Schematic illustration of the preparation of interfacial instability-driven PS-*b*-P4VP particles from evaporative emulsions using different organic solvents. Increasing solvent selectivity toward the P4VP block amplifies interfacial instability, leading to morphological transitions from spheres with inner pores to porous particles, vesicles, micelles, and micellar aggregates

Table 1 Calculated Hansen solubility parameters (δ, $MPa^{1/2}$) of solvents used in this work

Solvent	δ_t [a]	δ_d [b]	δ_p [c]	δ_h [d]
Cyclohexane	16.7	16.7	0	0
Toluene	18.2	18.0	1.4	2.0
Benzene	18.5	18.4	0	2.0
Chloroform	18.9	17.8	3.1	5.7
Dichloromethane	20.2	18.2	6.3	6.1
1-Hexanol	21.2	15.8	4.3	13.5
1-Pentanol	21.7	16.0	4.5	13.9
1-Butanol	23.2	16.0	5.7	15.8

[a]Total solubility parameter $\delta_t=(\delta_d^2+\delta_p^2+\delta_h^2)^{1/2}$

[b]Dispersive

[c]Polar

[d]Hydrogen bonding force

are 18.6 and 22.5 $MPa^{1/2}$, respectively [40, 41], the large contrast between P4VP and cyclohexane ($(\delta_{t,cyclohexane}-\delta_{P4VP})^2=33.64$) confirms a strong selectivity toward the PS block. This preference drives PS-*b*-P4VP chains to form micellar structures with P4VP cores and PS shells in organic solution [42, 43]. Upon solvent evaporation, the increasing BCP concentration induces chain reorganization near the oil/water interface. Co-adsorption of PS-*b*-P4VP and SDS at the droplet surface reduces the interfacial tension, initiating localized roughening and facilitating limited water penetration into the droplet interior [37]. However, the presence of pre-formed micelles with P4VP cores encapsulated by PS shells creates a high energy barrier for chain exchange, thereby restricting further adsorption and limiting the extent of water ingress.

As the solvent selectivity for P4VP increases from cyclohexane to benzene and toluene, the contrast in δ values decreases (i.e., $(\delta_{t,benzene}-\delta_{P4VP})^2=18.49$ and $(\delta_{t,toluene}-\delta_{P4VP})^2=16$). This reduction in selectivity relaxes the contraction of P4VP chains, enhancing their interfacial adsorption and amplifying surface roughness during evaporation. Consequently, pronounced porous textures emerge both on the surface and within the particles (Fig. 1c–f). The average pore sizes are 88.9 ± 25 nm for toluene and 93.3 ± 30 nm for benzene, respectively, which we refer to collectively as porous particles.

3.2 Effect of solvent selectivity: neutral solvent

Chloroform and dichloromethane (DCM) exhibit nearly balanced affinities for both PS and P4VP blocks, with calculated solubility parameter contrasts of $(\delta_{t,chloroform}-\delta_{PS})^2=0.09$ $MPa^{1/2}$, $(\delta_{t,chloroform}-\delta_{P4VP})^2=12.96$ $MPa^{1/2}$, $(\delta_{t,dichloromethane}-\delta_{PS})^2=2.56$ $MPa^{1/2}$, and $(\delta_{t,dichloromethane}-\delta_{P4VP})^2=5.29$ $MPa^{1/2}$, respectively [44]. This near-neutral selectivity promotes balanced solvation of both blocks and results in the formation of vesicular structures characterized by concentric P4VP-rich layers ranging from 100 to 300 nm in thickness (Fig. 2a–d). The enhanced solubility of P4VP in these solvents facilitates stronger interfacial adsorption of PS-*b*-P4VP at the oil/water boundary, leading to pronounced interfacial undulations and subsequent fragmentation of emulsion droplets into smaller vesicles. To visualize this transformation in real time, the structural evolution of DCM-based emulsions was monitored using differential interference contrast optical microscopy (Fig. 2e). Initially, complex water-in-oil-in-water (w/o/w) emulsions containing large aqueous inclusions were observed. As DCM gradually evaporated, pronounced interfacial roughening

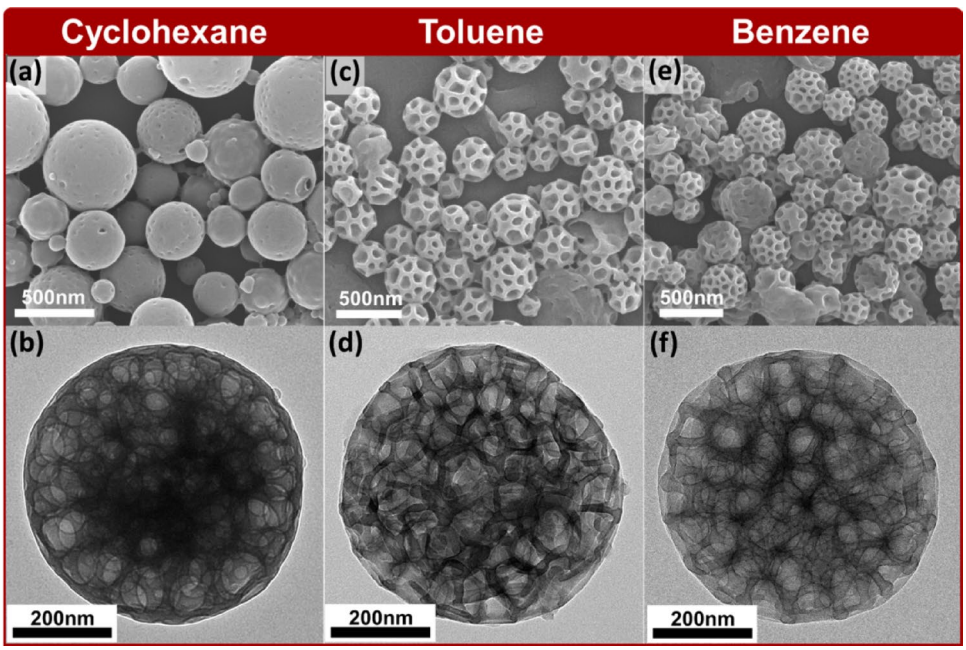

Fig. 1 **a**, **c**, **e** SEM and **b**, **d**, **f** TEM images of PS_{27k}-*b*-$P4VP_{7k}$ particles prepared using PS-selective solvents: **a**, **b** cyclohexane, **c**, **d** toluene, and **e**, **f** benzene

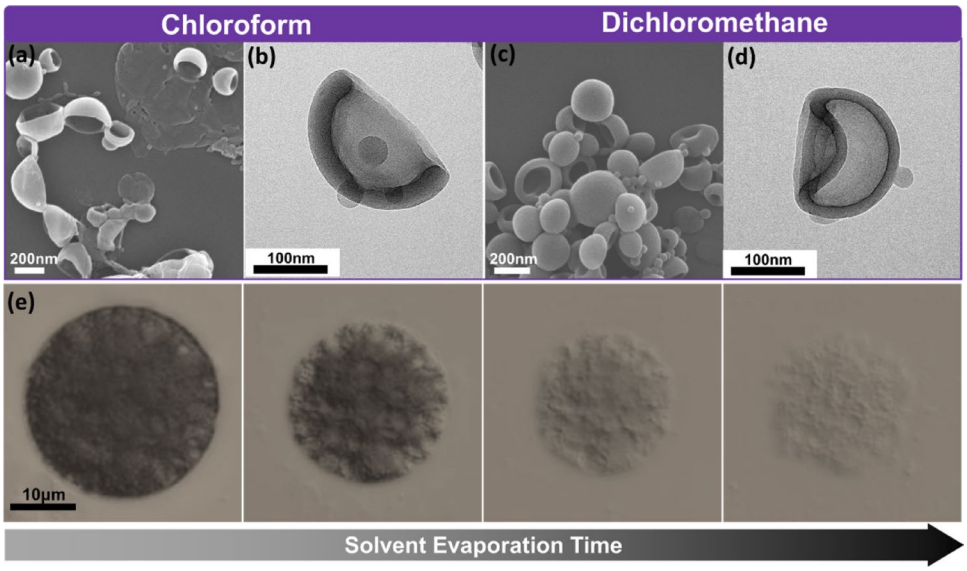

Fig. 2 **a**, **c** SEM and **b**, **d** TEM images of PS_{27k}-*b*-$P4VP_{7k}$ particles prepared using **a**, **b** chloroform and **c**, **d** dichloromethane, both exhibiting near-neutral selectivity toward PS and P4VP blocks; **e** Time-dependent evolution of vesicular structures from dichloromethane-based emulsions containing PS_{27k}-*b*-$P4VP_{7k}$

and droplet shrinkage occurred, eventually yielding stable vesicular structures consistent with the morphologies seen in SEM and TEM images (Fig. 2c, d).

This transition can be attributed to the cooperative effects of strong PS-*b*-P4VP adsorption and the intrinsically low interfacial tension between DCM (or chloroform) and water [37]. To further quantify this relationship, the interfacial tension (γ) between the BCP-containing organic phase (10 mg mL^{-1}) and the aqueous SDS solution (4 mg mL^{-1}) was measured using a pendant-drop tensiometer. Although these γ values represent equilibrium interfaces at a fixed BCP concentration (1 wt%) and thus may not fully capture solvent concentration gradients and viscosity changes during evaporation, they serve as thermodynamic indicators of the relative tendency toward interfacial instability, which correlates well with the observed morphological evolution. As summarized in Figure S3, the incorporation of PS-*b*-P4VP markedly lowers γ to below 0.8 $mN{\cdot}m^{-1}$, compared with 4.7 $mN{\cdot}m^{-1}$ for pure DCM at C_{SDS}=0.4 wt%. The effects of surfactant concentration and P4VP volume fraction on γ and resulting particle morphologies are analyzed in subsequent sections.

3.3 Effect of solvent selectivity: P4VP-selective solvent

Alcohol-based solvents serve as P4VP-selective media due to their ability to form hydrogen bonds with pyridyl moieties along the P4VP chains, thereby enhancing the preferential solvation of the hydrophilic block. Stable PS-*b*-P4VP emulsions can thus be generated using alcohols with alkyl chains equal to or longer than butyl, which are sufficiently immiscible with water to sustain the droplet interface. As shown in Fig. 3a, butanol-in-water emulsions stabilized with SDS yield distinct morphologies depending on C_{SDS}. At low C_{SDS} (<0.1 wt%), spherical micellar aggregates with an average diameter of 201 ± 30 nm are obtained. Voronoi analysis (Figure S4) reveals that these aggregates consist of hexagonally packed micellar subunits at the particle surface. Each micelle comprises a PS core and a P4VP shell, swollen through hydrogen bonding with butanol. During emulsification, butanol rapidly diffuses into the aqueous phase, while P4VP chains, enriched at the interface, entangle the micellar units to form supra-micellar aggregates [45]. As solvent evaporation proceeds, the networked micellar assembly solidifies, producing well-defined hexagonal surface arrays. The time-resolved formation of these hierarchical structures was examined by freeze-drying emulsions at controlled evaporation intervals (t_{evap} = 1, 4, 12, and 20 h) (Figure S5). Initially smooth particles (t_{evap} = 1 h) gradually develop surface roughness after 4 h, which propagates across the entire particle by 12–20 h, evidence of progressive micellar nucleation and coalescence during solvent loss. In particular, the C_{SDS} value plays a pivotal role in this process. Supra-micellar aggregation occurs predominantly at C_{SDS}<0.2 wt%, where stable micron-sized droplets are observed, with representative initial droplet diameters in the range of approximately 6 to 14 μm (Figure S6 a,b). In contrast, at higher surfactant levels (≥0.25 wt%), above the critical micelle concentration (CMC) of SDS, large emulsion droplets cannot be stably maintained under the same emulsification conditions, and the system is dominated by submicrometer droplets (Figure S6 c). This suppresses depletion interactions and leads to the formation of isolated core–shell micelles rather than aggregates.

The solvent transport dynamics in these emulsions involve two coupled processes: (i) solvent diffusion from the droplet interior to the continuous phase and (ii) solvent

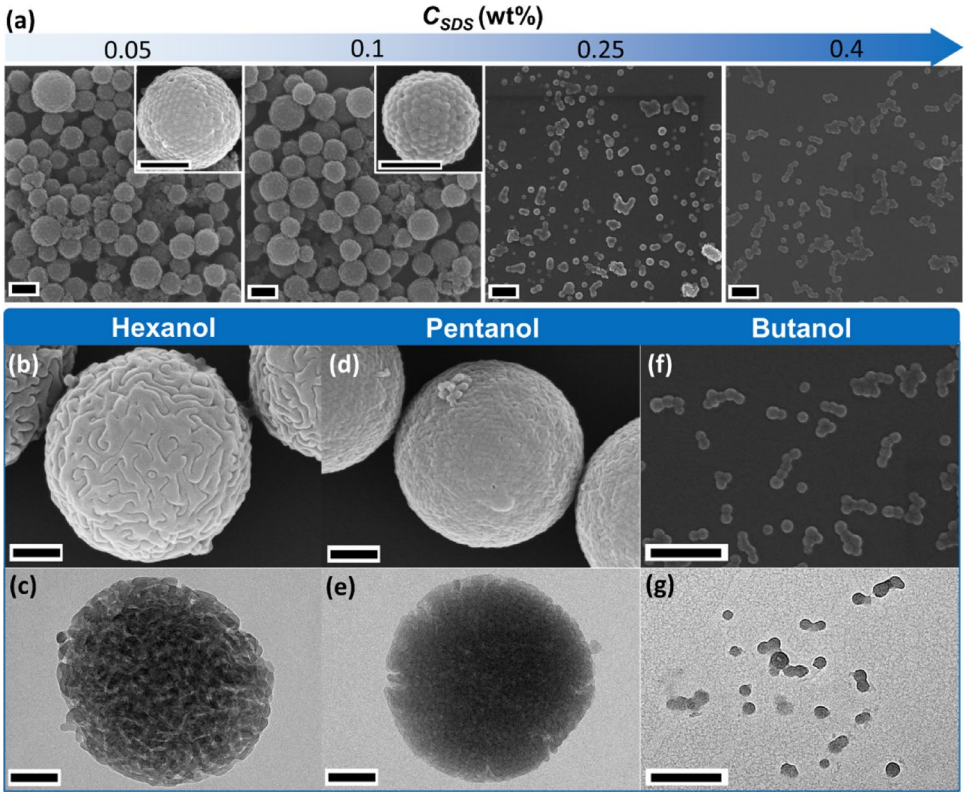

Fig. 3 **a** SEM images of PS_{27k}-*b*-$P4VP_{7k}$ micellar aggregates and micelles prepared from butanol-in-water emulsion at different SDS concentrations (C_{SDS}) of 0.05, 0.1, 0.25, and 0.4 wt%; (b, d, f) SEM and (c, e, g) HR-TEM images of PS_{27k}-*b*-$P4VP_{7k}$ particles prepared using alcohol solvents: **b**, **c** butanol, **d**, **e** pentanol, and **f**, **g** hexanol at a fixed C_{SDS} of 0.4 wt%. The scale bars are 200 nm

evaporation through the air/water interface. Consequently, the water miscibility of the chosen alcohol critically determines both the rate of solvent removal and the degree of micellar depletion within droplets. For example, butanol, partially miscible with water (63.2 gL^{-1} at 20 °C), facilitates rapid shrinkage and solidification of droplets [46]. In contrast, the lower solubilities of pentanol (22.0 gL^{-1} at 20 °C) and hexanol (5.9 gL^{-1} at 20 °C) slow down solvent exchange, leading to larger, more persistent emulsion droplets [47]. Figure 3b–g reveals the resulting morphologies from butanol, pentanol, and hexanol at a fixed C_{SDS}=0.4 wt%. While all samples produce micellar aggregates ranging from 200 nm to 1 µm, distinct surface textures are observed. Hexanol, exhibiting weaker hydrogen-bonding capability toward P4VP, generates rough, nonuniform surfaces composed of worm-like micelles. In contrast, butanol and pentanol favor the formation of well-ordered spherical micelles arranged in hexagonal arrays. These differences can be rationalized by the packing parameter of the swollen PS-*b*-P4VP chains, $p=v/a_0l_c$, where a_0 represents the contact area of the swelled P4VP, while v and l_c represent the volume and length of the PS block, respectively. In butanol and pentanol, extensive P4VP swelling decreases p below 1/3, stabilizing spherical micelles. Conversely, the weaker P4VP solvation in hexanol increases p to between 1/3 and 1/2, favoring cylindrical or worm-like micellar morphologies. Moreover, the lower water solubilities of pentanol and hexanol produce larger initial droplets (> 15 µm), sustaining sufficient depletion interactions to form micellar aggregates even at surfactant concentrations above the CMC.

3.4 Effect of f_{P4VP} and C_{SDS}

The geometric configuration of PS-*b*-P4VP assemblies at the oil/water interface, governed by the packing parameter (p), dictates both the surface undulation and the local organization of micellar subunits on the BCP particle. Accordingly, tuning the volume fraction of the hydrophilic P4VP block (f_{P4VP}) provides a powerful handle to control interfacial curvature and particle morphology [48]. To elucidate this effect, four PS-*b*-P4VP copolymers with systematically varied f_{P4VP} (*i.e.*, 0.12–0.50 by using PS_{40k}-*b*-$P4VP_{5.6k}$, PS_{27k}-*b*-$P4VP_{7k}$, PS_{15k}-*b*-$P4VP_{7k}$, and $PS_{9.8k}$-*b*-$P4VP_{10k}$) were examined in four representative solvents (*i.e.*, cyclohexane, benzene, dichloromethane, and butanol) under identical C_{SDS}=0.4 wt%. The resulting morphologies are summarized in Fig. 4. In cyclohexane, a strongly PS-selective solvent, spherical particles containing internal pores were observed for low f_{P4VP} samples (PS_{40k}-*b*-$P4VP_{5.6k}$ (f_{P4VP}=0.12) and PS_{27k}-*b*-$P4VP_{7k}$ (f_{P4VP}=0.2)), with mean pore diameters increasing from 25 to 87 nm (Fig. 4a, b). Further increase of f_{P4VP} to 0.32 produced well-developed porous particles (average pore ≈ 93 nm; Fig. 4c), while f_{P4VP}=0.50 yielded irregular, coalesced pores (100–300 nm; Fig. 4d). At higher f_{P4VP}, the

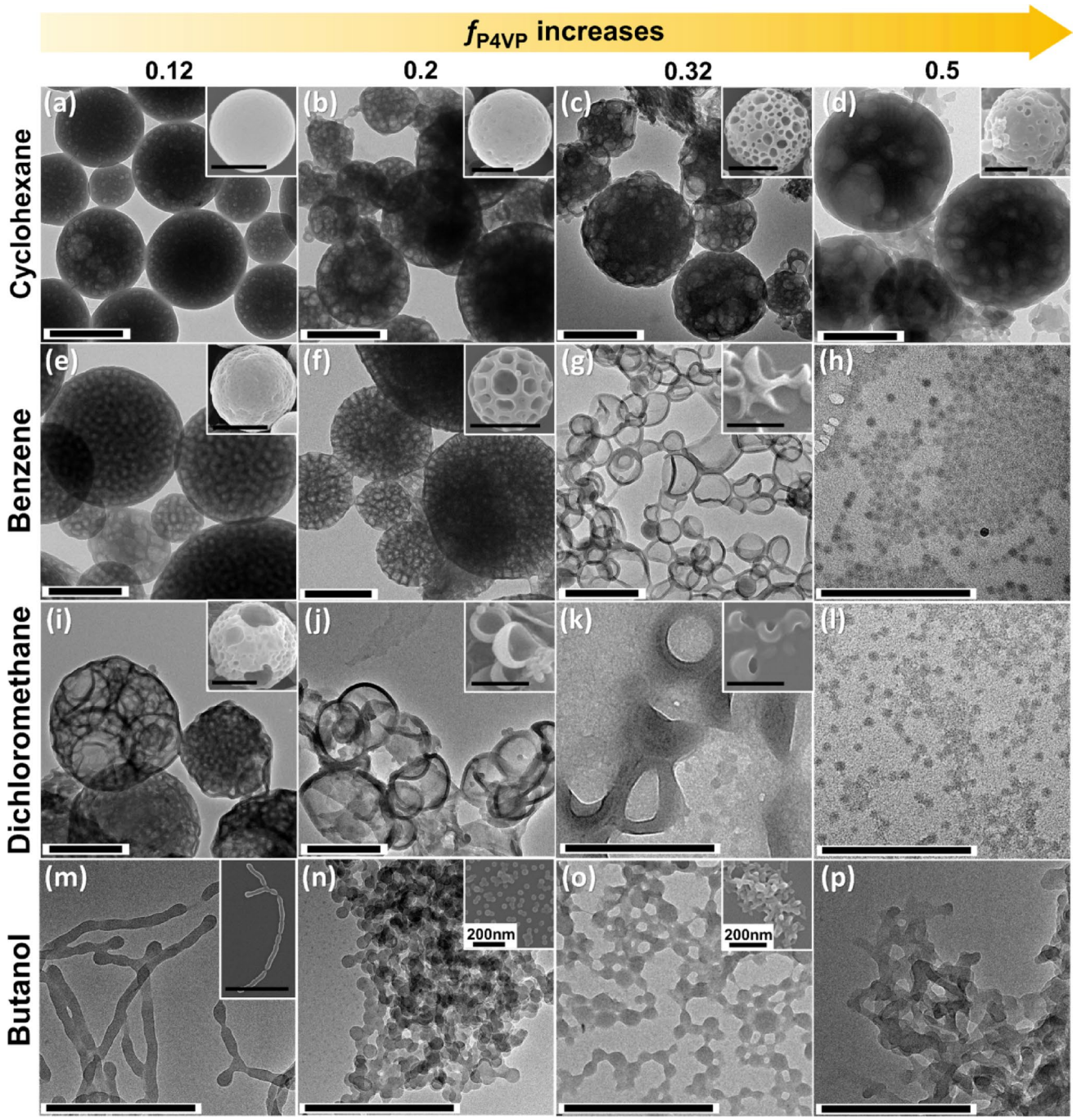

Fig. 4 TEM and SEM (inset) images of PS-*b*-P4VP particles with different molecular weights (*i.e.*, PS_{40k}-*b*-$P4VP_{5.6k}$, PS_{27k}-*b*-$P4VP_{7k}$, PS_{15k}-*b*-$P4VP_{7k}$, and $PS_{9.8k}$-*b*-$P4VP_{10k}$) prepared from **a**–**d** cyclohexane, **e**–**h** benzene, **i**–**l** dichloromethane, and **m**–**p** butanol emulsions. C_{SDS} is fixed at 0.4 wt%. The scale bars are 500 nm

poor compatibility between cyclohexane and P4VP retards chain mobility, producing kinetically trapped P4VP cores and a broad pore-size distribution during solvent evaporation [42].

When benzene was used, the system produced a broader morphological library: from spheres with inner pores to vesicles and micelles, as f_{P4VP} increased, similar to previous reports [37]. At $f_{P4VP}=0.12$, PS_{40k}-*b*-$P4VP_{5.6k}$ formed rough-surfaced spheres with internal pores (~52 ± 7 nm) (Fig. 4e). At $f_{P4VP}=0.32$, vesicular structures appeared, and at $f_{P4VP}=0.50$, discrete micelles dominated (Fig. 4g, h). This progressive transition reflects a decrease in interfacial curvature with increasing hydrophilic content. At low f_{P4VP} (≤0.20), only limited water penetrates the P4VP domains,

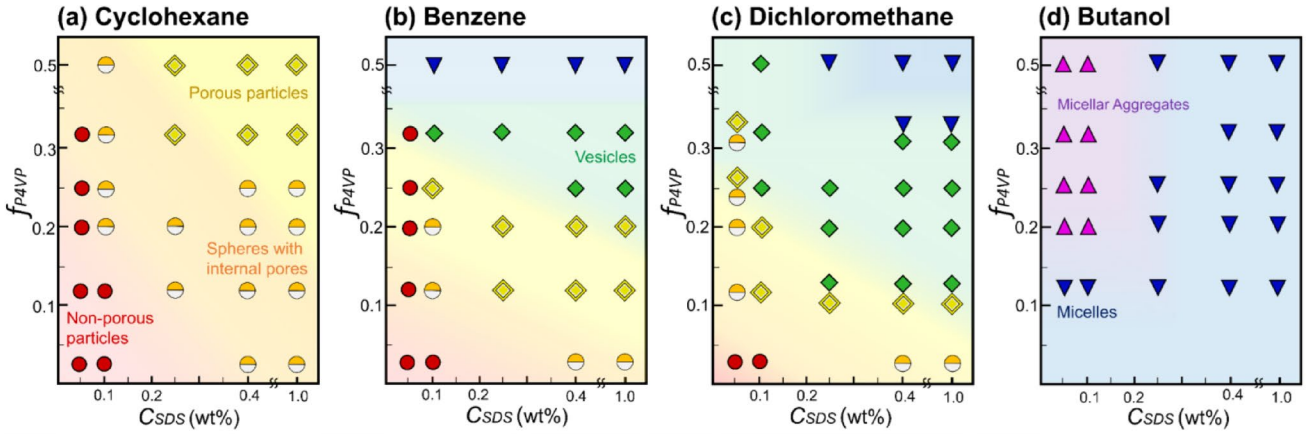

Fig. 5 Morphological phase diagram of PS-*b*-P4VP particles depending on f_{P4VP} and various SDS surfactant concentrations (C_{SDS}) prepared from different solvents of **a** cyclohexane; **b** benzene; **c** DCM; and **d** butanol. Each particle structure is denoted as follows: non-porous particles (●, red); spheres with internal pores (◓, orange); porous particles (◈, yellow); vesicles (◆, green); micelles (▼, blue) and micellar aggregates (▲, purple)

forming spherical particles with small internal cavities. Above f_{P4VP}=0.32, the water-swollen P4VP domains expand to exceed the PS volume, driving interfacial flattening and eventual release of BCP micelles into the aqueous phase, thus forming vesicles and isolated micelles [49]. The morphological sequence from spheres to vesicles corresponds well with the f_{P4VP}-dependent decrease in interfacial tension (γ), which drops from 3.9 to 2.1 mN·m^{-1} across these structures (Figure S3). This continuous reduction in γ indicates enhanced P4VP chain swelling and adsorption at the interface, promoting stronger interfacial instability and progressive morphological diversification. In DCM, similar f_{P4VP}-dependent transitions occur but at lower f_{P4VP} thresholds than in benzene (Fig. 4i–l). Even the least hydrophilic composition (f_{P4VP}=0.12) yields large internal pores (~200 nm), owing to the moderate solvation of both blocks and enhanced interfacial adsorption of swollen P4VP chains. As f_{P4VP} increases to 0.32 and 0.50, vesicles and micelles emerge as interfacial instability intensifies.

Distinct behavior arises in butanol-in-water emulsions, where the strong P4VP selectivity of butanol fundamentally alters the assembly pathway. At f_{P4VP}=0.12, the swollen chains adopt a packing parameter p between 1/3 and 1/2, producing worm-like micelles composed of PS cores and P4VP shells (Fig. 4m). Increasing f_{P4VP} beyond 0.20 reduces p below 1/3 as the P4VP domains swell further, stabilizing spherical micelles arranged into hexagonal aggregates (Fig. 4n–p). Thus, the morphological evolution with f_{P4VP} in alcohol-based emulsions can be rationalized by hydrogen-bond-mediated P4VP swelling, which continuously modulates p and hence the preferred interfacial curvature. A consistent trend is observed for other alcohol solvents, where micellar aggregates persist but their subunit geometry transitions from cylindrical to spherical with increasing f_{P4VP} (Figure S7).

As discussed above, sequential shape transitions of BCP particles from spheres with inner pores to porous particles, vesicles, and micelle structures, are achieved upon increasing interfacial instability. The key governing parameters are the solvent type, C_{SDS}, and f_{P4VP}, each of which modulates the extent of interfacial adsorption and roughening at the emulsion boundary. To map the combined influence of these parameters, particle morphologies were systematically examined as a function of C_{SDS} and f_{P4VP} across the four solvent systems, and the resulting phase diagrams are summarized in Fig. 5a–d (corresponding TEM images in Figures S8-S11). The C_{SDS} varied from 0.05 to 1.0 wt%, while two additional polymers, PS_{116k}-*b*-$P4VP_{4k}$ (f_{P4VP}=0.03) and PS_{51k}-*b*-$P4VP_{18k}$ (f_{P4VP}=0.25), were incorporated to extend the compositional range. We also note that the conditions at f_{P4VP}=0.5 and C_{SDS}=0.05 wt% did not yield well-defined or reproducible particles due to emulsion instability and were therefore excluded from the morphological analysis.

Due to hydrogen bonding between 4VP units and water, water acts as a swelling solvent for the P4VP block. In addition, the formation of P4VP–SDS complexes at the oil–water interface further increases the effective hydrophilicity and water affinity of the P4VP block [28], while SDS simultaneously serves as an emulsion stabilizer at the oil/water interface. At low C_{SDS}, where interfacial tension remains relatively high, the interaction between P4VP and SDS is weak, resulting in limited interfacial adsorption and a low degree of interfacial instability. Consequently, nonporous spherical particles (*i.e.*, red circle) are obtained regardless of solvent type. As C_{SDS} increases, however, cooperative co-adsorption of SDS and PS-*b*-P4VP at the droplet interface becomes more pronounced. The combined reduction

in interfacial tension and enhanced hydration of the P4VP block increases its affinity for the aqueous phase, promoting higher interfacial curvature and amplifying interfacial instability.

Each structural regime in the phase diagram thus reflects a specific threshold of interfacial destabilization dictated by f_{P4VP} and C_{SDS}. For instance, in cyclohexane (Fig. 5a), particles evolve from smooth spheres to porous architectures as both C_{SDS} and f_{P4VP} increase, consistent with stronger interfacial perturbation. In benzene and DCM (Fig. 5b, c), a broader spectrum of morphologies emerges, including porous particles, vesicles, and micelles, demonstrating the synergistic control of hydrophilic content and surfactant loading over curvature and interfacial dynamics. In contrast, butanol (Fig. 5d) consistently yields micellar and micellar-aggregate structures due to its high P4VP selectivity and intrinsically low interfacial tension; here, the dominant hydrogen-bonding interactions favor micelle formation even at $C_{SDS} \leq 0.1$ wt %. When C_{SDS} exceeds ~ 0.2 wt%, excess SDS molecules predominantly form micelles in the aqueous phase rather than further adsorbing at the interface or interacting with P4VP. As a result, the interfacial tension remains nearly unchanged with further increases in C_{SDS}, and no significant additional morphological transitions are observed. This behavior is consistent with the known CMC of SDS (~ 0.23 wt%). Overall, the constructed morphological phase diagrams establish a coherent framework linking molecular composition, solvent polarity, and interfacial energy to the hierarchical self-assembly pathways of amphiphilic PS-*b*-P4VP.

4 Conclusions

In conclusion, this study elucidates how interfacial-instability-driven self-assembly of amphiphilic PS-*b*-P4VP BCPs can be harnessed to construct structurally diverse colloidal particles with programmable architectures. By systematically tuning solvent selectivity, surfactant concentration, and P4VP composition, we establish quantitative design rules that link molecular interactions to interfacial curvature, tension reduction, and morphological evolution. Hydrophilic solvent environments and higher f_{P4VP} promote pronounced interfacial adsorption and roughening, leading to a continuous transformation from porous spheres to vesicles and micellar assemblies. The resulting morphological phase diagrams unify these dependencies into a comprehensive framework for predicting and controlling solvent-mediated BCP self-assembly. This approach offers a robust and scalable route for creating hierarchically organized polymer particles, paving the way for tailored materials in photonic, catalytic, and bio-responsive applications.

Supplementary Information The online version contains supplementary material available at https://doi.org/10.1007/s13233-025-00488-2.

Acknowledgements This research was supported by the National Research Foundation of Korea (NRF) grant, funded by the Korean Government (2022R1C1C1006324). We thank UNIST Office of Research Facilities and Training (ResFacT) for support of using the equipment.

Funding Open Access funding enabled and organized by Ulsan National Institute of Science and Technology (UNIST)

Data availability The data that support the findings of this study are available from the corresponding author upon reasonable request.

Declarations

Conflict of interest The authors declare no competing financial interest.

References

1. X. Zhao, F. Pan, H. Xu, M. Yaseen, H. Shan, C.A.E. Hauser, S. Zhang, J.R. Lu, Chem. Soc. Rev. **39**, 3480 (2010). https://doi.org/10.1039/b915923c
2. P. Kumari, M.K. Bera, S. Malik, B.K. Kuila, ACS Appl. Mater. Interfaces **7**, 12348 (2015). https://doi.org/10.1021/am507266e
3. T. Shimizu, M. Masuda, H. Minamikawa, Chem. Rev. **105**, 1401 (2005). https://doi.org/10.1021/cr030072j
4. J.W. Lee, J.H. Kim, D.J. An, J.K. Lee, N. Kim, S.H. Kim, Macromol. Res. **27**, 974 (2019). https://doi.org/10.1007/s13233-020-8013-4
5. J. Baettig, J. Oh, J. Bang, A. Khan, Macromol. Res. **25**, 1091 (2017). https://doi.org/10.1007/s13233-017-5142-5
6. T.H. Zhao, G. Jacucci, X. Chen, D.-P. Song, S. Vignolini, R.M. Parker, Adv. Mater. **32**, 2002681 (2020). https://doi.org/10.1002/adma.202002681
7. H. Cui, Z. Chen, S. Zhong, K.L. Wooley, D.J. Pochan, Science **317**, 647 (2007). https://doi.org/10.1126/science.1141768
8. S. Yang, W. Qin, X. Zhao, F. He, H. Liu, Q. Zhou, J. Huang, G. Yu, Y. Feng, J. Li, J. Colloid Interface Sci. **645**, 580 (2023). https://doi.org/10.1016/j.jcis.2023.04.165
9. C.-S. Lim, J.H. Heo, M.S. You, S.H. Im, K.J. Chae, Macromol. Res. **22**, 324 (2014). https://doi.org/10.1007/s13233-014-2047-4

10. L. Navarro, A.F. Thünemann, T. Yokosawa, E. Spiecker, D. Klinger, Angew. Chem. Int. Ed. **134**, e202208084 (2022). https://doi.org/10.1002/anie.202208084
11. K.H. Ku, J.M. Shin, H. Yun, G.-R. Yi, S.G. Jang, B.J. Kim, Adv. Funct. Mater. **28**, 1802961 (2018). https://doi.org/10.1002/adfm.201802961
12. M. Radjabian, V. Abetz, Prog. Polym. Sci. **102**, 101219 (2020). https://doi.org/10.1016/j.progpolymsci.2020.101219
13. R. Deng, L. Zheng, X. Mao, B. Li, J. Zhu, Small **17**, 2006132 (2021). https://doi.org/10.1002/smll.202006132
14. Z. Tan, S. Ban, Y. Ahn, K.H. Ku, B.J. Kim, Chem. Sci. **16**, 6265 (2025). https://doi.org/10.1039/d5sc00259a
15. Q. He, K.H. Ku, H. Vijayamohanan, B.J. Kim, T.M. Swager, J. Am. Chem. Soc. **142**, 10424 (2020). https://doi.org/10.1021/jacs.0c02398
16. J. Lee, S. Ban, K. Jo, H.S. Oh, J. Cho, K.H. Ku, ACS Nano **18**, 5196 (2024). https://doi.org/10.1021/acsnano.4c00230
17. E.J. Kim, J.M. Shin, Y. Kim, K.H. Ku, H. Yun, B.J. Kim, Polym. Chem. **10**, 2415 (2019). https://doi.org/10.1039/C9PY00306A
18. S.-J. Jeon, G.-R. Yi, S.-M. Yang, Adv. Mater. **20**, 4103 (2008). https://doi.org/10.1002/adma.200801377
19. N. Yan, H. Liu, Y. Zhu, W. Jiang, Z. Dong, Macromolecules **48**, 5980 (2015). https://doi.org/10.1021/acs.macromol.5b01219
20. D. Hu, Y. Wang, J. Liu, Y. Mao, X. Chang, Y. Zhu, Nanoscale **14**, 6291 (2022). https://doi.org/10.1039/D2NR01172G
21. K. Jo, J. Lee, J. Cho, K.H. Ku, Macromolecules **58**, 3038 (2025). https://doi.org/10.1021/acs.macromol.5c00064
22. S. Ban, J. Lee, H. Kim, K.H. Ku, ACS Appl. Mater. Interfaces **17**, 41154 (2025). https://doi.org/10.1021/acsami.5c09465
23. J. Zhu, R.C. Hayward, J. Am. Chem. Soc. **130**, 7496 (2008). https://doi.org/10.1021/ja801268e
24. Z. Wang, Y. Cao, X. Zhang, D. Wang, M. Liu, Z. Xie, Y. Wang, Langmuir **32**, 13517 (2016). https://doi.org/10.1021/acs.langmuir.6b03940
25. S. Lee, J.J. Shin, K.H. Ku, Y.J. Lee, S.G. Jang, H. Yun, B.J. Kim, Macromolecules **53**, 7198 (2020). https://doi.org/10.1021/acs.macromol.0c01004
26. J. Lee, H.S. Oh, S. Ban, J. Cho, K.H. Ku, Angew. Chem. Int. Ed. (2025). https://doi.org/10.1002/anie.202511262
27. Q. Yu, N. Sun, D. Hu, Y. Wang, X. Chang, N. Yan, Y. Zhu, Y. Li, Polym. Chem. **12**, 4184 (2021). https://doi.org/10.1039/D1PY00744K
28. C. Li, W. Wang, X. Wang, H. Jiang, J. Zhu, S. Lin, Eur. Polym. J. **68**, 409 (2015). https://doi.org/10.1016/j.eurpolymj.2015.05.011
29. J. Bae, J. Lawrence, C. Miesch, A. Ribbe, W. Li, T. Emrick, J. Zhu, R.C. Hayward, Adv. Mater. **24**, 2735 (2012). https://doi.org/10.1002/adma.201200570
30. R.H. Staff, D. Schaeffel, A. Turshatov, D. Donadio, H.-J. Butt, K. Landfester, K. Koynov, D. Crespy, Small **9**, 3514 (2013). https://doi.org/10.1002/smll.201300372
31. T. Higuchi, K. Motoyoshi, H. Sugimori, H. Jinnai, H. Yabu, M. Shimomura, Macromol. Rapid Commun. **31**, 1773 (2010). https://doi.org/10.1002/marc.201000299
32. J.M. Shin, Y. Kim, H. Yun, G.-R. Yi, B.J. Kim, ACS Nano **11**, 2133 (2017). https://doi.org/10.1021/acsnano.6b08342
33. H. Yoon, M. Choi, K.J. Lee, J. Jang, Macromol. Res. **16**, 85 (2008). https://doi.org/10.1007/bf03218836
34. J.K. Kim, J.I. Lee, D.H. Lee, Macromol. Res. **16**, 267 (2008). https://doi.org/10.1007/BF03218519
35. S.I. Yoo, B.-H. Sohn, Macromol. Res. **24**, 292 (2016). https://doi.org/10.1007/s13233-016-4027-3
36. R.S. Kurusu, N.R. Demarquette, Eur. Polym. J. **89**, 129 (2017). https://doi.org/10.1016/j.eurpolymj.2017.02.016
37. K.H. Ku, J.M. Shin, D. Klinger, S.G. Jang, R.C. Hayward, C.J. Hawker, B.J. Kim, ACS Nano **10**, 5243 (2016). https://doi.org/10.1021/acsnano.6b00985
38. L. Li, K. Matsunaga, J. Zhu, T. Higuchi, H. Yabu, M. Shimomura, H. Jinnai, R.C. Hayward, T.P. Russell, Macromolecules **43**, 7807 (2010). https://doi.org/10.1021/ma101529b
39. H. Yu, X. Qiu, S.P. Nunes, K.-V. Peinemann, Nat. Commun. **5**, 4110 (2014). https://doi.org/10.1038/ncomms5110
40. K.H. Ku, Y. Kim, G.-R. Yi, Y.S. Jung, B.J. Kim, ACS Nano **9**, 11333 (2015). https://doi.org/10.1021/acsnano.5b05058
41. S. O'Driscoll, G. Demirel, R.A. Farrell, T.G. Fitzgerald, C. O'Mahony, J.D. Holmes, M.A. Morris, Polym. Adv. Technol. **22**, 915 (2011). https://doi.org/10.1002/pat.1596
42. H.-i Shin, B.G. Min, W. Jeong, C. Park, Macromol. Rapid Commun. **26**, 1451 (2005). https://doi.org/10.1002/marc.200500290
43. K.-S. Kim, S. Jang, S.I. Yoo, B.-H. Sohn, Macromol. Res. **26**, 182 (2018). https://doi.org/10.1007/s13233-018-6017-0
44. T.P. Lodge, B. Pudil, K.J. Hanley, Macromolecules **35**, 4707 (2002). https://doi.org/10.1021/ma0200975
45. T. Yang, Z. Lei, S. Yang, E.-Q. Chen, Phys. Chem. Chem. Phys. **21**, 2121 (2019). https://doi.org/10.1039/C8CP06679E
46. B.G. Harvey, H.A. Meylemans, J. Chem. Technol. Biotechnol. **86**, 2 (2011). https://doi.org/10.1002/jctb.2540
47. S. Song, H. Zhou, M. Puzhitsky, Y. Zhang, G. Hicks, Y. Lu, I. Manners, M.A. Winnik, Macromolecules **54**, 930 (2021). https://doi.org/10.1021/acs.macromol.0c02521
48. Y. Lee, J.-B. Chang, H.K. Kim, T.G. Park, Macromol. Res. **14**, 359 (2006). https://doi.org/10.1007/BF03219095
49. G.M. Nabar, J.O. Winter, B.E. Wyslouzil, Soft Matter **14**, 3324 (2018). https://doi.org/10.1039/C8SM00425K

Authors and Affiliations

Juyoung Lee[1] · Hayoung Kim[1] · Hyeong Seok Oh[1] · Kang Hee Ku[1]

✉ Kang Hee Ku
kangheeku@unist.ac.kr

[1] School of Energy and Chemical Engineering, Ulsan National Institute of Science and Technology (UNIST), Ulsan 44919, Republic of Korea